Non-Invasive High-Throughput Metrology of Functionalized Graphene Sheets

Maziar Ghazinejad, Jennifer Reiber Kyle, Shirui Guo, Dennis Pleskot, Duoduo Bao, Valentine I. Vullev, Mihrimah Ozkan, and Cengiz S. Ozkan**

The utilization of fluorescence quenching microscopy (FQM) for quick visualization of chemical functionalization in relatively large regions of graphene, grown via chemical vapor deposition (CVD), is discussed. Through reactive ion plasma etching, patterns of p-type CVD-grown graphene functionalized with fluorine are generated. 4-(dicyanomethylene)-2-methyl-6-(4-dimethylaminostyryl)-4H-pyran (DCM) is used as the fluorescent agent. The emission of DCM is quenched to a different extent by fluorinated and pristine graphene, which provides the fluorescence-imaging contrast essential for this metrology. To probe the functionalized surface patterns with DCM, the dye is dispersed in polymethylmethacrylate (PMMA) then the graphene surface is coated, forming a 30-nm-thick DCM-PMMA layer. Fluorescence images of dye-coated graphene distinctly reveal the difference between the chemically treated and as-grown regions. The pristine graphene quenches the DCM emission more efficiently than the fluorinated graphene. Therefore, the regions with pristine graphene appear darker on the fluorescence images than the regions with fluorinated graphene, enabling large-scale mapping of the functionalized regions in CVD grown graphene sheets Due to its simplicity and consistent results, FQM is now poised for widespread adoption by graphene manufacturers as a basis for facile and high throughput metrology of large-scale graphene sheets.

1. Introduction

Development of novel materials offers unique technical solutions that occasionally change the very nature of an industrial field. In the semiconductor technology, a standard example of such trend, fabrication and implementation of new devices relied heavily on innovative materials solutions. Successful development of such solutions often calls for new metrology techniques to provide feedback to the fabrication process and, accordingly, improve targeted performance of the new materials. Graphene is a carbon allotrope that has been hailed as the latest prodigy of nanotechnology, and eventually claimed a Noble prize in Physics.[1] This sensation is primarily due to graphene's fascinating and versatile properties, such as high charge carrier mobility, unique band structure, mechanical robustness, high thermal transport, and chemical stability.[2–8] As a result, a considerable amount of theoretical and experimental research has focused on investigating potential applications of graphene nanostructures in field-effect transistors, actuators, solar cells, batteries, and sensors.[9–12] For graphene, however, to successfully transition from a gifted child into an accomplished adult that delivers its promises, it still needs to become relevant at industrially-usable scales. Recent experimental studies on graphene synthesis point to promising approaches, such as CVD, for fabricating large-area graphene sheets.[13–17] So far, the electronic attributes of graphene stand out as one of its greatest selling points and have been the subject of most of graphene research efforts. Such attractive features include high charge carrier mobility,[18] unique band structure,[19] and unconventional quantum hall effect.[4,20] Recently, graphene-based field-effect transistors (GFETs) have been introduced as a prospect for post-silicon electronics.[21,22] For fabrication of devices and interconnects, however, the electrical properties of graphene need to be modulated. Chemical doping, a major approach for tuning electronic properties, has been consistently applied in semiconductor materials to control the type and density of charge carriers.[23,24] A variety of chemical methods have been reported for functionalizing graphene to n- and p-type, which are required for complementary metal oxide semiconductor (CMOS) materials and, accordingly, logic circuits.[25] As the graphene processing methods develop, the need for high-throughput metrology techniques, capable of mapping functionalized areas on a large scale, keeps recurring.[23,24,26,27]

Characterization techniques such as electron microscopy, scanning probe microscopy, Raman spectroscopy, and X-ray

M. Ghazinejad, D. Pleskot, Prof. C. S. Ozkan
Departments of Mechanical Engineering and Bioengineering
Materials Science and Engineering Program
University of California
Riverside, CA 92521 USA
E-mail: cozkan@engr.ucr.edu

J. R. Kyle, S. Guo, Prof. M. Ozkan
Departments of Electrical Engineering and Chemistry
University of California
Riverside, CA 92521 USA
E-mail: mihri@ee.ucr.edu

D. Bao, Prof. V. Vullev
Department of Bioengineering
University of California
Riverside, CA 92521 USA

DOI: 10.1002/adfm.201200434

photoemission spectroscopy allow measurement of specific properties against metrics of interest, including defects, uniformity, and Fermi level. While these techniques provide valuable information about electronic and structural properties of graphene at an atomic-level, they are often slow and encompass only small regions. For example, mapping a 1cm^2 graphene sheet with a coarse mesh of 1 point per 100 μm requires 10 000 measurements. Because each collection point requires about 30–60 s, such a measurement would take around 150 h.

Fluorescence quenching microscopy (FQM) has been successfully utilized in biomedical and materials research.[28,29] Recent advances in FQM have demonstrated its promising potential for characterization of graphene materials.[27,30,31] Recognizing the benefit of a high-throughput optical metrology, a few studies focused on exploiting graphene's photophysical properties to visualize it.[27,32–34]

Treossi et al. utilized fluorescence quenching to visualize graphene on surfaces functionalized with quaterthiophene.[33] Considering the electron-donating properties of quaterthiophene,[35] and the Fermi energy of graphene[36] the authors ascribed the observed quenching to photo-induced charge transfer,[33] which is a short-range process requiring electronic coupling between the graphene and the fluorescent thiophene dye.

Concurrently, Kim et al. developed a FQM technique, which allows for visualization of sheets of exfoliated graphene, graphene oxide and reduced graphene oxide deposited on arbitrary substrates.[27,30] The authors applied polymer layers doped with fluorescent dyes, over the graphene sheets.[27] The dye selection was governed by the overlap between their emission spectra and the absorption of graphene materials, allowing for quenching induced by resonance energy transfer with considerable efficiency at distances exceeding 10 nm. The long-range quenching mechanism of this FQM approach allows for using multilayers of dye molecules (doped in the polymer matrix), and hence for attaining high-contrast discernibility between the different graphene substrates that were imaged.[27,30]

Sun et al. employed the FQM method developed by Kim et al. for imaging the graphane/graphene patterns.[31] The difference between the quenching propensity of graphene and graphane yielded a pronounced FQM contrast.[31]

Recently, we extended FQM to a graphene-metrology technique by automatically quantifying the extent of fluorescence quenching via image processing. The automated determination of quenching allowed us to achieve centimeter-scale metrology of layer thickness and uniformity of entire CVD-grown graphene sheets.[37] In contrast to the current sequential characterization techniques that record one data point at a time, FQM technique provides high-throughput identification of graphene, up to diffraction limit, at a single recording.[27,37]

Herein, we demonstrate the capability of our FQM metrology to visually differentiate regions of chemically functionalized and pristine graphene. Through analysis of the fluorescence image histograms, we calculate distinctive intensity ranges that correspond to functionalized and as-grown graphene. Spectroscopic studies of photo-physical properties of the dye revealed that an increase in non-radiative decay rates in the presence of graphene were the principal reason for the observed emission quenching. We also improve upon the FQM image segmentation algorithm by implementing Gaussian curve fitting to dynamically determine the contrast ranges corresponding to graphene regions. This work represents a significant augmentation for FQM; since in addition to its ability to determine layers and homogeneity of large-scale graphene, it can now visualize and map chemically functionalized regions in CVD-grown graphene sheets.

2. Results and Discussion

Chemical functionalization of graphene often results in disruption of sp^2-hybridization of carbon atoms, change in Fermi level, and accordingly, change in the excitation energy of graphene.[25,38,39] Therefore, we expect FQM to allow identification of chemically treated graphene through reduced quenching.

We performed chemical functionalization through fluorination of graphene via reactive ion plasma etching since it allows generation of complex functionalization patterns through lithography techniques. Fluorination of graphene offers a practical route for the optical and electronic modifications needed for a number of graphene device applications.[38,40] Following the procedure outlined in[41], we fluorinated selected areas of CVD-grown graphene sheets with CF_4 plasma and striped protective masks. The graphene samples were then coated by a DCM–PMMA solution, as described in our previous work.[37]

To visualize functionalized regions of CVD graphene, we collected FQM images of fluorinated CVD graphene (**Figure 1**). Fluorinated and pristine regions of the CVD graphene sample were detectable in the original collected large-area fluorescence montage; however, individual images had dark outlines due to uneven illumination (Figure 1a). It should be noted that large-area fluorescence montage image allows for unbounded large-scale mapping of the graphene sample without compromising the necessary resolution. Using a low-magnification objective would deteriorate mapping resolution. Furthermore, there is a limit to the area that even a very low-magnification objective can image. Flat-field correction was used to remove the effect of uneven illumination in the individual images, resulting in a uniform large-area image (Figure 1b). In FQM, regions are identified by their intensity contrast relative to the unquenched fluorescence peak in the image histogram.[37] Contrast between two regions in fluorescence quenching is given by:

$$C_{2-1} = \frac{I_1 - I_2}{I_1} \quad (1)$$

When region 1 is the bare glass substrate, which does not quench the dye layer fluorescence emission, contrast is equal to the fluorescence quenching factor of graphene in region 2. The original FQM image segmentation algorithm applied fixed contrast ranges to all FQM images for identifying graphene layers. These contrast ranges were experimentally determined. In this work, we improve upon the FQM image segmentation algorithm by implementing Gaussian curve fitting to automatically and dynamically determine the contrast ranges corresponding to graphene regions. To perform Gaussian curve fitting, the user enters the rough location of the image histogram peaks and the height, width, and location parameters of the histogram-fitted

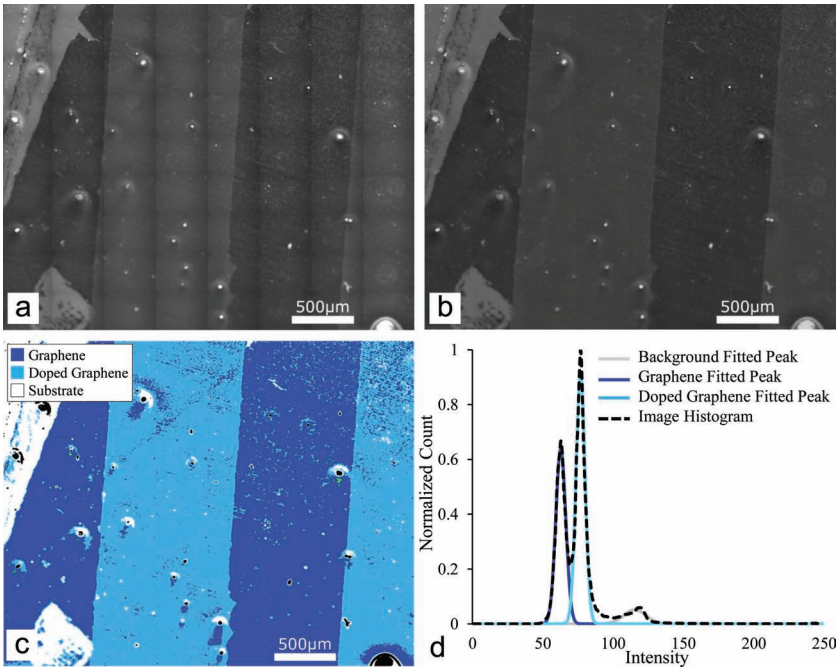

Figure 1. Fluorescence images of CVD graphene fluorinated using a striped mask a) before and b) after flat-field correction. c) Fluorescence quenching metrology segmented image showing the pristine graphene regions (dark blue) and fluorinated graphene regions (light blue). d) The fluorescence image histogram and fitted Gaussian peaks corresponding to the substrate (grey), fluorinated graphene (light blue), and pristine graphene (dark blue).

Gaussian curves are automatically determined. Our algorithm utilizes the "fminsearch" function provided by MATLAB to fit the Gaussian curves to the histogram peaks. The fminsearch function implements the Nelder-Mead simplex method.[42,43] The Nelder-Mead algorithm is an iterative function-minimization method, in our case employed to minimize the error function measured between the Gaussian curve to be fitted and the image histogram.

Our segmentation algorithm segments the FQM image by mapping pixels within the image to regions according to their intensity contrast relative to the background signal, taken as the location of the Gaussian curve fitted to the substrate fluorescence intensity peak in the image histogram. Contrast ranges corresponding to segmented regions are bounded at the intensity values where the fitted Gaussian curves overlap. This algorithm successfully segments the corrected FQM image into pristine graphene, fluorinated graphene, glass substrate, and contamination (black) regions (Figure 1c). The contrast (C) ranges, determined from Gaussian curve fitting of the fluorescence image histogram (Figure 1d), are: $-0.2 \leq C < 0.217$–substrate, $0.217 \leq C < 0.391$–fluorinated single-layer graphene, $0.391 \leq C < 0.58$–pristine single-layer graphene, and $C < -0.2$, $C > 0.58$–contamination.

Contrast between pristine graphene and the substrate, measured between the peaks of the fitted Gaussian curves, is 48%. This value is in agreement with the results from the original FQM segmentation algorithm, published previously.[37] Contrast between fluorinated graphene and the substrate is reduced to 32% and contrast between fluorinated graphene and pristine graphene is 23%.

In FQM, not all of the fluorophores in the dye layer are quenched by graphene. Therefore, the measured fluorescence emission is a combination of signals from quenched and unquenched fluorophores. As quenching increases, the ratio of quenched fluorophores to unquenched fluorophores increases. The emission peak height attenuation indicates this ratio. Comparing peak heights in fluorescence emission spectra of the dye layer over the bare substrate, fluorinated graphene, and pristine graphene, we find that peak height attenuation by fluorinated graphene is approximately 25% of attenuation by pristine graphene (**Figure 2**a). Therefore, while both fluorinated and pristine graphene quench fluorescence emission, quenching potency of fluorinated graphene has been noticeably reduced. Upon fluorination the absorptivity of graphene, and thus the spectral overlap with emission of DCM, decreased (Figure 2b).When quenching occurs due to charge transfer mechanism, its efficiency and FQM image would strongly depend on change in Fermi level and type of chemical doping. Conversely, when the quenching occurs due to energy transfer mechanism its efficiency is primarily affected by absorptivity.[44]

To demonstrate the efficacy of FQM for visualizing complex chemical functionalization patterns, we used a high-resolution circular photolithography mask to fluorinate a CVD graphene sample and collected FQM images of the fluorinated sample. The fluorinatation pattern is readily visible in the original fluorescence image (**Figure 3**a) and segmentation (preceded by flat-field correction) accurately maps functionalized and pristine regions (Figure 3b). In this sample, contrast between fluorinated graphene and pristine graphene (determined from fitted Gaussian curve locations) is only 17%, which is smaller than the 23% contrast observed in the sample fluorinated using the simple striped mask (Figure 1). This reduced contrast between the fluorinated and pristine regions indicates reduced chemical

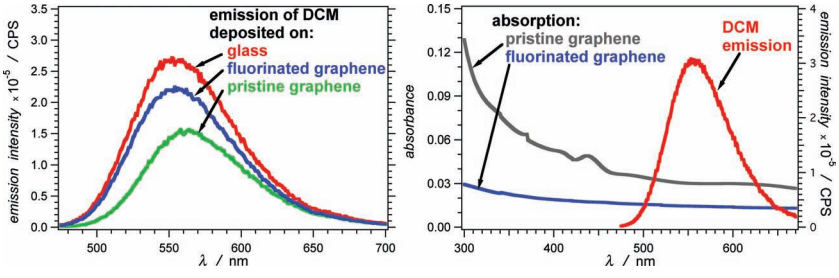

Figure 2. a) Fluorescence spectra of the 30-nm DCM-PMMA (1% w/w) layer over bare glass, fluorinated graphene, and pristine graphene (λ_{ex} = 460 nm). b) Overlap of the emission spectrum of DCM-PMMA film with the absorption spectra of pristine and fluorinated graphene.

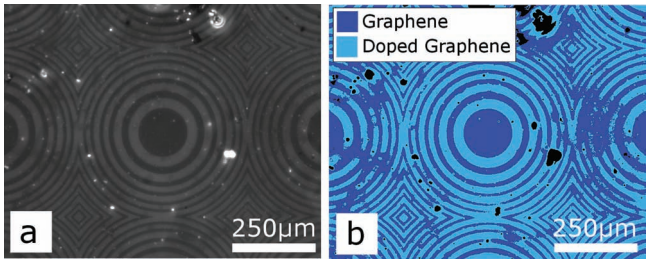

Figure 3. a) Original fluorescence and b) fluorescence quenching metrology-segmented images of CVD graphene fluorinated using a circle mask.

treatment efficacy with the complex circular pattern. Unlike graphene layers, which always have the same quenching contrast, fluorinated regions have variable quenching contrast due to variations in the fluorination intensity. Therefore, a segmentation algorithm cannot identify chemically modified regions using fixed contrast ranges. However, because our segmentation algorithm uses Gaussian curve fitting to automatically determine dynamic contrast ranges, the fluorinated regions are accurately identified and mapped in the segmented image (Figure 3b).

To investigate the change in graphene structure due to chemical functionalization we employed Raman spectroscopy technique.[45] Raman spectroscopy allows for resolving bonding patterns in graphene sheets and offers insight on the changes in electronic state and structure of graphene due to chemical and electrical doping.[46–48]

A typical Raman spectrum collected from our CVD-grown graphene sheet is shown in **Figure 4**. The G band, centered on 1580 cm^{-1}, is the first-order Raman mode induced by in-plane vibration of carbon atoms in sp^2-hybridized graphene sheets. As a result, the intensity and sharpness of G band signify the presence of crystalline graphitic phase in the synthesized material. The D band at 1335c m^{-1} is the defect-originated second-order Raman band which indicates the level of disorder in graphitic sp^2 structures. The nature of this band is related to

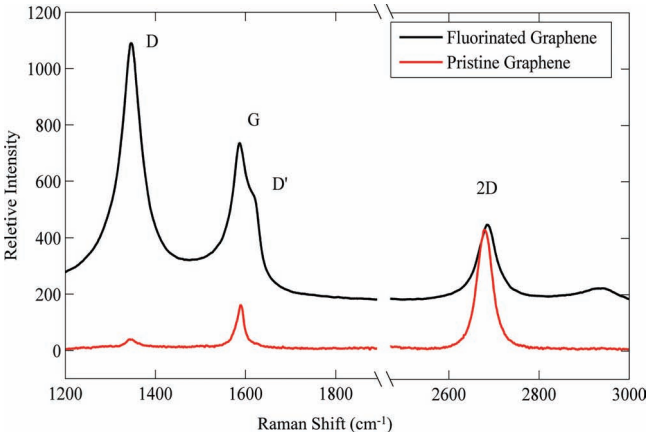

Figure 4. Raman spectra of pristine (bottom) and fluorinated (top) graphene (λ_{ex} = 532 nm).

one-phonon elastic scattering and it is interpreted as a measure of the quantity of sp^3 or dangling sp^2 bonds that are causing structural disorders. The 2D-band at 2600 cm^{-1}, on the other hand, is originated by an inelastic scattering processes that involve phonons. This band is sensitive to the number of layers and is more pronounced in single- to few-layer graphene. Thus, a 2D/G intensity ratio has been consistently used to determine the thickness of graphene sheets. The collected Raman spectra verify that the CVD-grown graphene sheet has a very low defect level and is primarily single- to bi-layer.

Several studies on carbon nanotubes and carbon bulk materials showed that formation of sp^3 bonds, which are produced from breaking of the sp^2 network in graphene, contributes to an increase in the D peak intensity.[38,47,48] As a result, any type of chemical doping, or process in general, that yields such a distortion in hybridization of carbon atoms would affect the ratio of D band to G band peak intensities, I_D/I_G. We observed that the intensity of the D peak of fluorinated graphene was much larger than that of the G and 2D peaks, and therefore I_D/I_G ratio increased considerably. Because the D peak represents transitions between vibrational states associated with the sp^3 defects, its presence indicates an increase in the degree of disorder. The ratio of 2D band and G band peak, I_{2D}/I_G, is also susceptible to chemical doping, as it generally reduces 2D band intensity.[36,47,48] Thus, while chemical doping usually escalates I_D/I_G, it reduces I_{2D}/I_G.[36,49] Such behavior was echoed by the Raman spectra that we collected from the fluorinated graphene sample (Figure 4).

To characterize the quenching of the DCM fluorescence by graphene, we employed UV/visible spectroscopy. Comparison between the steady-state emission spectra of PMMA-DCM films coated on bare glass and on glass-immobilized graphene showed a decrease in the fluorescence intensity of the dye in the presence of the carbon allotrope (Figure 2a). Correcting for the amount of light absorbed, as estimated from the absorbance of the dye in the polymer films, revealed that pristine graphene caused almost two fold decrease in the emission quantum yield of DCM, Φ_f, in comparison with the samples on bare glass (**Table 1**). Concurrently, the emission quantum yield of DCM dispersed in a polymer film coated over fluorinated graphene was larger than Φ_f in presence of pristine graphene but still smaller than Φ_f for the films on bare glass (Table 1). Thus, the fluorinated graphene did not quench the DCM emission as efficiently as the pristine graphene, which was consistent with our observations with the fluorescence microscopy (Figure 1, Figure 3).

To quantify the DCM excited-state kinetics and elucidate the processes responsible for the observed fluorescence quenching, we resorted to time-resolved emission spectroscopy. The lack of linearity in the decays of the intensity of the DCM emission, when plotted against logarithmic ordinate (**Figure 5**), indicated that the deactivation of the emissive excited state of the dye did not have a mono-exponential character. This observation was consistent with the heterogeneity of the solid samples, requiring multi-exponential analysis. As previously reported in,[50] bi-exponential functions provided the simplest mathematical expression that could successfully fit the emission decays of DCM (Table 1). The average lifetimes, $\langle\tau\rangle$, obtained from the bi-exponential fits, manifested a similar trend as the emission

Table 1. Photophysical properties of DCM coatings of glass and graphene samples.[a)]

sample	Φ_f	τ_1[b)] [ns (f_1)]	τ_2[b)] [ns (f_2)]	$\langle\tau\rangle$[c)] [ns]	$k_r \times 10^{-8}$[d)] [s^{-1}]	$k_{nr} \times 10^{-8}$ [e)] [s^{-1}]	$k_Q \times 10^{-8}$ [f)] [s^{-1}]
Bare Glass	0.72	1.82 (0.69)	3.65 (0.31)	2.69	2.7	1.0	0
Fluorinated Graphene	0.57	1.33 (0.66)	3.40 (0.34)	2.49	2.1	1.9	0.9
Pristine Graphene	0.39	1.13 (0.74)	2.90 (0.26)	1.96	2.0	3.1	2.1

[a)]DCM was dispersed in PMMA, and the dye-doped polymer was deposited as 30–nm thick films on bare glass, and on glass-immobilized single-sheet graphene samples; [b)]From exponential fits of TCSPC-measured emission decays: λ_{ex} = 406 nm (pulse half-height width = 195 ps); λ_{ex} = 566 nm; [c)]Average lifetime: $\langle\tau\rangle = (f_1\tau_1^2 + f_2\tau_2^2)/(f_1\tau_1 + f_2\tau_2)$; [d)]Apparent radiative-decay rate constant: $k_r = \Phi_f/\langle\tau\rangle$; [e)]Apparent non-radiative-decay rate constant: $k_{nr} = (1-\Phi_f)/\langle\tau\rangle$; [f)]Apparent emission-quenching rate constant: $k_Q = k_{nr} - k_{nr}^{(\text{bare glass})}$.

quantum yields (Table 1). While $\langle\tau\rangle$ of DCM deposited over bare glass was 2.69 ns, $\langle\tau\rangle$ of DCM in the presence of pristine graphene was 1.96 ns (Table 1).

From Φ_f and $\langle\tau\rangle$ we estimated the rate constants of the radiative, k_f, and non-radiative, k_{nr}, processes responsible for the deactivation of the DCM excited state (Table 1). Graphene had a relatively small effect on k_f. For samples with and without graphene, the values of k_f varied within about 30%, from 2.0×10^8 s^{-1} to 2.7×10^8 s^{-1} (Table 1), which was expected since graphene should not affect the electronic structure of the DCM molecules in order to alter its radiative decay rates. The carbon allotropes, however, considerably affected the non-radiative decay rates. The presence of pristine graphene caused a three-fold increase in k_{nr} in comparison with the sample of dye-polymer films deposited on bare glass (Table 1). These findings allowed us to estimate the apparent pseudo-monomolecular quenching rate constants, k_Q: 2.0×10^8 s^{-1} and 8.4×10^8 s^{-1} for pristine and fluorinated graphene, respectively (Table 1).

Our photophysical findings, considered along with the structural properties of the samples, suggested that the observed emission quenching resulted predominantly from resonance energy transfer.[51–53] Processes requiring at least adequate electronic coupling between the dye and the graphene, such as charge transfer and electron-exchange energy transfer, are inefficient at donor-acceptor distances exceeding about two nanometers.[54] Considering the 30-nm-thick coated polymer-dye layer, measured by a surface profilometer, such electron-transfer processes would be unfeasible for more than 90% of the DCM molecules in the polymer film, and hence could not explain the observed 46% decrease in Φ_f in the presence of graphene (Table 1). Conversely, the donor-acceptor distances at which Förster resonance energy transfer (FRET) is efficient are comparable with the thickness of the dye-doped polymer films that we used. Furthermore, fluorination of the pristine graphene decreases its absorptivity in the spectral region where DCM emits. Concurrently, k_Q for fluorinated graphene was more than twice smaller than k_Q for pristine graphene (Table 1), which was consistent with a decrease in the FRET rate as a result lowering the molar extinction coefficient upon fluorination of the graphene, which was the energy acceptor.

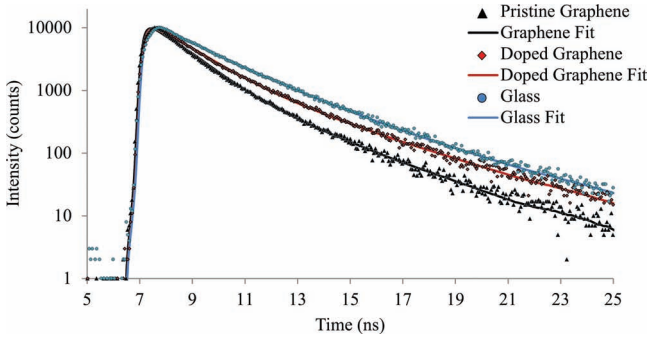

Figure 5. Fluorescence decays of 30-nm DCM-PMMA layer (1% w/w) over bare glass, fluorinated graphene, and pristine graphene. λ_{ex} = 406 nm (pulse half-height width = 195 ps); λ_{em} = 566 nm.

3. Conclusions

After the first development of fluorescence quenching microscopy for metrology of centimeter-scale CVD-grown graphene sheets, we are still exploring different capabilities of the method. Given that our approach is based on quenching phenomena, investigating the parameters involved in graphene quenching enables us to methodically realize versatile potentials of this new promising metrology technique. Herein, we demonstrate the aptitude of FQM for accurately visualizing chemically functionalized regions in graphene sheets. Our inspiration for this work was the modifications that functionalization processes cause on the chemical and electronic state of their subject materials. This, in turn, alters the fluorescence quenching condition of chemically modified graphene, compared to that of pristine graphene. Such variation would visually differentiate functionalized and pristine areas of graphene when viewed under a fluorescence microscope.

In this work, first we successfully show the functionality of large-scale FQM in mapping of fluorinated regions in graphene sheets. To determine the method's resolution and scalability strength, we increased the complexity of the fluorination pattern and successfully reproduced the mapping results. Upon that, we conducted a comparative investigation on steady-state and time-resolved fluorescence parameters of dye-coated pristine graphene and fluorinated graphene, using bare glass as the control sample. The fluorometry results support the increasing trend observed in the quenching level of DCM dye, from control sample to fluorinated graphene to pristine graphene. The variation in fluorescence quenching by graphene after it is fluorine treated is also predicted by theory, as discussed in this

report. Finally, we improved our image processing technique by employing Gaussian fitting to determine the contrast regions corresponding to graphene regions. This is a valuable improvement since it facilitates the automation of the technique for production-line metrology of graphene.

The presented results imply that FQM metrologies is indeed beyond a simple fluorescence imaging technique and can visually distinguish between pristine and chemically processed regions in a very same CVD-grown sheet. This work also suggests that, with premeditated choice of dye, the interaction between fluorophores and graphene provides advantages for probing the chemical structure of functionalized graphene over large areas. Due to its simplicity, high speed, and small footprint, segmented FQM can be employed to address the chronic need for a microscopy based graphene metrology capable of "seeing" the features that are processed.

4. Experimental Section

Graphene Growth: 2 5 μm-thick copper foils (from Alfa Aesar, cut into 1cm^2) were chosen as the catalyst substrate. The copper foil was etched with acetic acid at 35 °C for 10 min to remove any copper oxide on the foil's surface. After washing the foils completely with deionized (DI) water, they were loaded into a CVD chamber and heated them to 1000 °C under 5-Torr pressure. Once the temperature was stabilized at 1000 °C, the catalyst substrates (foils) were annealed for 30 min under a 100/100 sccm flow of hydrogen and argon gas. Next, the argon feed was stopped and a methane gas flow of 100 sccm was introduced into the tube for 20 minutes to begin the chemical vapor deposition of graphene on copper. All flow rates were precisely controlled using mass flow controllers. Upon completion of the CVD growth, methane gas feed were stopped and the furnace was cooled to room temperature under the protection of argon gas flow. Graphene sheets, grown on copper foils, were removed from the CVD chamber, covered with PMMA by spin coating, and heated at 100 °C for 10 min to bake the PMMA layer. Next, the graphene sheets were removed from the copper film by etching in a 0.3 M aqueous $FeCl_3$ solution, followed by rinsing with an aqueous HCl (4%) and DI water solution. Graphene samples were then allowed to relax on the glass substrates overnight before they were dipped in acetone to remove the PMMA layer.[37]

Graphene Fluorination: For patterned fluorination, a CVD graphene sheet immobilized on a glass substrate was spin-coated with a photoresist layer. Next, photolithography was performed using a patterned mask having circular and stripe windows to define the areas to be fluorine-treated. Upon development of the mask, graphene sheets were selectively fluorinated using a reactive ion etching (RIE) machine. The plasma treatment was carried out at room temperature with the CF_4 gas pressure fixed at 10 mTorr, while the CF_4 flow rate was kept constant at 50 sccm. Graphene fluorination was performed with 10 s of plasma exposure at an RF power level of 25W.[41] After dissolving the photoresist in acetone overnight, selectively fluorinated graphene was dried and prepared for dye coating.

Dye Preparation and Coating: The fluorescent dye mixture consisted of 1 wt% PMMA (M_w = 120 000) and 0.01 wt% 4-(dicyanomethylene)-2-methyl-6-(4-dimethylaminostyryl)-4H–pyran (DCM Sigma-Aldrich) in toluene (>99.5% Fisher Chemical). The dye solution was stirred and heated overnight to dissolve the polymer, then continuously kept stirring while stored. Immediately before the solution was spun onto the substrate it was sonicated for 15 min, and passed through a 0.22 μm filter to ensure homogeneity of the dye solution and to avoid unnecessary contamination. The polymer-dye was then spin-coated onto the surface of the graphene at 3000 rpm for 60 s. The thickness of coated dye-polymer layer is 30 nm, measured with Dektak 8 Surface Profilometer. Once coated, the graphene was placed in a desiccator for at least 1 h to ensure the complete evaporation of the solvent and maintain a consistent layer thickness of the dye on different graphene samples.

Fluorescence Microscopy: A BD Pathway 855 HT confocal microscope with an arc lamp light source was used to acquire the images. The light path of the incident light consisted of a 470 nm bandpass filter and a 520 nm dichroic filter. The light then passed through an Olympus 20× objective lens with 0.75 NA and was emitted through a 542 nm bandpass filter before being detected by a CCD camera. The final images were produced using a montage of smaller images that captured 417 × 318 μm^2 sections of the sample in order to maintain high resolution over a large area. The images were obtained with the help of BD AttoVision software.

Emission and Absorption Spectroscopy: Diffuse reflectance spectroscopy allowed us to obtain UV/visible absorption spectra of the solid-film samples using a JASCO V-670 spectrophotometer (Tokyo, Japan), equipped with a 60 mm ψ integrating sphere equipped with an individual detector (Model ISN-723, JASCO, Japan). Aluminum foil was used as a reflector for the blank slides and for all the samples. The absorbance, $A = -2\log(R)$, was determined from the reflectance, R, where the factor 2 was added to account for the reflector on the back of the transparent substrates.

Steady-state emission spectra and time-resolved emission decays were recorded using a FluoroLog-3 spectrofluorometer (Horiba-Jobin-Yvon) equipped with double-grating monochromators and a TBX single-photon-counting detector. Small-angle fluorescence spectroscopy settings allowed for collecting the emission signal at 22-degree angle from the incident excitation light.[55] From the steady-state absorption and emission data we calculated the fluorescence quantum yields.[56] Rhodamine 3B (R3B) was used as a standard: Φ_f of R3B in ethanol is 0.45.[57]

For recording the emission decays, we used the time-correlated single-photon counting (TCSPC) setup of the spectrofluorometer, employing pulsed diode laser for excitation source (406 nm, half-height pulse width = 195 ps). Bi-exponential data fits, involving deconvolution of the emission decay data, yielded the lifetimes, τ_i, and the corresponding weighing pre-exponential coefficients, f_i (Table 1).[58]

Image Processing: All image processing was performed using custom scripts in MATLAB v7.4. For flat-field correction, the following flat-field correction algorithm was applied to each individual image in the large-area fluorescence montage:

$$I_{\text{flat}}(x, y) = \frac{I_{\text{original}}(x, y)}{I_{\text{correction}}(x, y)} \times \overline{I_{\text{correction}}} \quad (2)$$

The correction image used in this algorithm has the same dimensions as the original individual images to be corrected and was taken of the bare substrate using the same optical settings used to collect the large-area montage.[37]

Acknowledgements

M.G. and J.R.K. contributed equally to this work. The authors gratefully acknowledge financial support for this work by the CMMI Division of the National Science Foundation (Award: 0800680), the Materials Research Science and Engineering Center (NSF-MRSEC) on Polymers (Award: 0213695), the Nanoscale Science and Engineering Center (NSF-NSEC) on Hierarchical Manufacturing (CHM, Award: 0531171), The Winston Chung Global Energy Center, National Science Foundation (CBET 0935995), and the Riverside Public Utilities. First author also gratefully acknowledges the American Public Power Association DEED grant. The authors also would like to thank Dr. David Carter from the Center for Plant Cell Biology at the University of California Riverside for helpful discussions on fluorescence imaging and Dr. Ali Guvenc for helpful discussions and support on image processing.

Received: February 11, 2012
Revised: May 6, 2012
Published online: July 6, 2012

[1] The Nobel Prize in Physics, http://nobelprize.org., 2012, 2010, (accessed November 2011).
[2] K. S. Novoselov, A. K. Geim, S. V. Morozov, D. Jiang, M. I. Katsnelson, I. V. Grigorieva, S. V. Dubonos, A. A. Firsov, *Nature* **2005**, *438*, 197.
[3] K. S. Novoselov, A. K. Geim, S. V. Morozov, D. Jiang, Y. Zhang, S. V. Dubonos, I. V. Grigorieva, A. A. Firsov, *Science* **2004**, *306*, 666.
[4] Y. Zhang, Y.-W. Tan, H. L. Stormer, P. Kim, *Nature* **2005**, *438*, 201.
[5] A. K. Geim, K. S. Novoselov, *Nat. Mater.* **2007**, *6*, 183.
[6] J.-H. Chen, C. Jang, S. Xiao, M. Ishigami, M. S. Fuhrer, *Nat. Nanotechnol.* **2008**, *3*, 206.
[7] A. A. Balandin, S. Ghosh, W. Bao, I. Calizo, D. Teweldebrhan, F. Miao, C. N. Lau, *Nano Lett.* **2008**, *8*, 902.
[8] C. Lee, X. Wei, J. W. Kysar, J. Hone, *Science* **2008**, *321*, 385.
[9] F. Schedin, A. K. Geim, S. V. Morozov, E. W. Hill, P. Blake, M. I. Katsnelson, K. S. Novoselov, *Nat. Mater.* **2007**, *6*, 652.
[10] X. Wang, L. Zhi, K. Mullen, *Nano Lett.* **2007**, *8*, 323.
[11] J. Yan, T. Wei, B. Shao, Z. Fan, W. Qian, M. Zhang, F. Wei, *Carbon* **2009**, *48*, 487.
[12] E. Yoo, J. Kim, E. Hosono, H.-s. Zhou, T. Kudo, I. Honma, *Nano Lett.* **2008**, *8*, 2277.
[13] A. Reina, X. Jia, J. Ho, D. Nezich, H. Son, V. Bulovic, M. S. Dresselhaus, J. Kong, *Nano Lett.* **2008**, *9*, 30.
[14] X. Li, W. Cai, J. An, S. Kim, J. Nah, D. Yang, R. Piner, A. Velamakanni, I. Jung, E. Tutuc, S. K. Banerjee, L. Colombo, R. S. Ruoff, *Science* **2009**, *324*, 1312.
[15] M. P. Levendorf, C. S. Ruiz-Vargas, S. Garg, J. Park, *Nano Lett.* **2009**, *9*, 4479.
[16] S. Bae, H. Kim, Y. Lee, X. Xu, J.-S. Park, Y. Zheng, J. Balakrishnan, T. Lei, H. Ri Kim, Y. I. Song, Y.-J. Kim, K. S. Kim, B. Ozyilmaz, J.-H. Ahn, B. H. Hong, S. Iijima, *Nat. Nanotechnol.* **2010**, *5*, 574.
[17] V. Singh, D. Joung, L. Zhai, S. Das, S. I. Khondaker, S. Seal, *Prog. Mater. Sci.* **2011**, *56*, 1178.
[18] X. Du, I. Skachko, A. Barker, E. Y. Andrei, *Nat. Nanotechnol.* **2008**, *3*, 491.
[19] A. H. Castro Neto, F. Guinea, N. M. R. Peres, K. S. Novoselov, A. K. Geim, *Rev. Mod. Phys.* **2009**, *81*, 109.
[20] K. S. Novoselov, E. McCann, S. V. Morozov, V. I. Fal'ko, M. I. Katsnelson, U. Zeitler, D. Jiang, F. Schedin, A. K. Geim, *Nat. Phys.* **2006**, *2*, 177.
[21] Y. M. Lin, C. Dimitrakopoulos, K. A. Jenkins, D. B. Farmer, H. Y. Chiu, A. Grill, P. Avouris, *Science* **2010**, *327*, 662.
[22] F. Schwierz, *Nat. Nanotechnol.* **2010**, *5*, 487.
[23] A. C. Diebold, *Handbook of Silicon Semiconductor Metrology*, CRC Press, Boca Raton, FL **2001**.
[24] D. K. Schroder, Semiconductor Material And Device Characterization, John Wiley and Sons, New York **2006**.
[25] H. Liu, Y. Liu, D. Zhu, *J. Mater. Chem.* **2010**, *21*, 3335.
[26] ITRS, in *The International Technology Roadmap for Semiconductors,* http://www.itrs.net, **2010**.
[27] J. Kim, L. J. Cote, F. Kim, J. Huang, *J. Am. Chem. Soc.* **2009**, *132*, 260.
[28] K. M. Cromheeke, M. M. Kockx, G. R. Y. De Meyer, J. M. Bosmans, H. Bult, W. J. F. Beelaerts, C. J. Vrints, A. G. Herman, *Cardiovasc. Res.* **1999**, *43*, 744.
[29] M. E. Kose, R. J. Crutchley, M. C. DeRosa, N. Ananthakrishnan, J. R. Reynolds, K. S. Schanze, *Langmuir* **2005**, *21*, 8255.
[30] J. Kim, F. Kim, J. Huang, *Mater. Today* **2010**, *13*, 28.
[31] Z. Sun, C. L. Pint, D. C. Marcano, C. Zhang, J. Yao, G. Ruan, Z. Yan, Y. Zhu, R. H. Hauge, J. M. Tour, *Nat. Commun.* **2012**, *2*, 559.
[32] A. Reina, S. Thiele, X. Jia, S. Bhaviripudi, M. Dresselhaus, J. Schaefer, J. Kong, *Nano Res.* **2009**, *2*, 509.
[33] E. Treossi, M. Melucci, A. Liscio, M. Gazzano, P. Samori, V. Palermo, *J. Am. Chem. Soc.* **2009**, *131*, 15576.
[34] C. M. Nolen, G. Denina, D. Teweldebrhan, B. Bhanu, A. A. Balandin, *ACS Nano* **2011**, *5*, 914.
[35] J. Wan, A. Ferreira, W. Xia, C. H. Chow, K. Takechi, P. V. Kamat, G. Jones II, V. I. Vullev, *J. Photochem. Photobiol. A* **2008**, *197*, 364.
[36] C. N. R. Rao, A. K. Sood, K. S. Subrahmanyam, A. Govindaraj, *Angew. Chem. Int. Ed.* **2009**, *48*, 7752.
[37] J. R. Kyle, A. Guvenc, W. Wang, M. Ghazinejad, J. Lin, S. Guo, C. S. Ozkan, M. Ozkan, *Small* **2011**, *7*, 2599.
[38] J. T. Robinson, J. S. Burgess, C. E. Junkermeier, S. C. Badescu, T. L. Reinecke, F. K. Perkins, M. K. Zalalutdniov, J. W. Baldwin, J. C. Culbertson, P. E. Sheehan, E. S. Snow, *Nano Lett.* **2010**, *10*, 3001.
[39] R. Saito, M. Yagi, T. Kimura, G. Dresselhaus, M. S. Dresselhaus, *J. Phys. Chem. Solids* **1999**, *60*, 715.
[40] W.-K. Lee, J. T. Robinson, D. Gunlycke, R. R. Stine, C. R. Tamanaha, W. P. King, P. E. Sheehan, *Nano Lett.* **2011**, *11*, 5461.
[41] S. Guo, M. Ghazinejad, X. Qin, H. Sun, W. Wang, F. Zaera, M. Ozkan, S. C. Ozkan, *Small* **2011**.
[42] R. A. Mead, J. A. Nelder *Comput. J.* **1965**, *7*, 308.
[43] J. C. Lagarias, A. R. James, H. W. Margaret, E. W. Paul, *SIAM J. Optimization* **1998**, *9*, 112.
[44] K. A. Velizhanin, A. Efimov, *Phys. Rev. B* **2011**, *84*, 085401.
[45] A. C. Ferrari, J. C. Meyer, V. Scardaci, C. Casiraghi, M. Lazzeri, F. Mauri, S. Piscanec, D. Jiang, K. S. Novoselov, S. Roth, A. K. Geim, *Phys. Rev. Lett.* **2006**, *97*, 187401.
[46] D. M. Basko, S. Piscanec, A. C. Ferrari, *Phys. Rev. B* **2009**, *80*, 165413.
[47] A. C. Ferrari, *Solid State Commun.* **2007**, *143*, 47.
[48] L. Zhao, R. He, K. T. Rim, T. Schiros, K. S. Kim, H. Zhou, C. Gutiérrez, S. P. Chockalingam, C. J. Arguello, L. Pálová, D. Nordlund, M. S. Hybertsen, D. R. Reichman, T. F. Heinz, P. Kim, A. Pinczuk, G. W. Flynn, A. N. Pasupathy, *Science 333*, 999.
[49] X. Dong, D. Fu, W. Fang, Y. Shi, P. Chen, L.-J. Li, *Small* **2009**, *5*, 1422.
[50] S. L. Bondarev, V. N. Knyukshto, V. I. Stepuro, A. P. Stupak, A. A. Turban, *J. Appl. Spectrosc.* **2004**, *71*, 194.
[51] G. Gomez-Santos, T. Stauber, *Phys. Rev. B* **2011**, *84*, 165438.
[52] R. S. Swathi, K. L. Sebastian, *J. Chem. Phys.* **2008**, *129*, 054703.
[53] R. S. Swathi, K. L. Sebastian, *J. Chem. Phys.* **2009**, *130*, 086101.
[54] J. R. Lakowicz, *Principles of Fluorescence Spectroscopy*, SpringerBoston, MA **2006**, Ch. 9.
[55] J. Wan, M. Thomas, S. Guthrie, V. Vullev, *Ann. Biomed. Eng.* **2009**, *37*, 1190.
[56] J. Hu, B. Xia, D. Bao, A. Ferreira, J. Wan, G. Jones, V. I. Vullev, *J. Phys. Chem. A* **2009**, *113*, 3096.
[57] R. F. Kubin, A. N. Fletcher, *J. Lumin.* **1983**, *27*, 455.
[58] H. Lu, D. Bao, M. Penchev, M. Ghazinejad, V. I. Vullev, C. S. Ozkan, M. Ozkan, *Adv. Sci. Lett.* **2010**, *3*, 101.